Influence of mesoporous substrate morphology on the structural, optical and electrical properties of RF sputtered ZnO layer deposited over porous silicon nanostructure

Yogesh Kumar, J. Escorcia García, Fouran Singh, S.F. Olive-Méndez, V.V. Sivakumar, D. Kanjilal, V. Agarwal.

Abstract

Morphological, optical and transport characteristics of the RF sputtered zinc oxide (ZnO) thin films over the mesoporous silicon (PS) substrates have been studied. Effect of substrate porosity on the grain growth and transport properties of ZnO has been analyzed. Physical and optical properties of ZnO–PS structures were investigated using scanning electron microscopy (SEM), X-ray diffraction (XRD), atomic force microscopy (AFM), and photoluminescence (PL) spectroscopy. Our experimental results indicate that on changing porosity of the PS substrates, regularity of the spatial distribution of the ZnO nanocrystallites can be controlled. While the morphology and grain size of ZnO depended strongly on the morphology and pore size of the PS substrates, the rectifying factors of the metal semiconductor junction were found to be different by a factor of 3. The deposition of semiconducting oxides on such mesoporous substrates/templates offers the possibility to control their properties and amplify their sensing response.

Keywords: Zin oxide, Porous silicon, RF sputtering, Mesoporous templates, Optical properties, Transport, Morphology.

Introduction

Semiconducting oxides have been known for their sensitivity in various sensor applications [1–3], exploiting their different properties such as the change of conductivity due to the adsorption or desorption of gases [4]. Furthermore, these materials can be grown in thin films allowing to minimize the size of the devices and to integrate themselves with the silicon technology [5]. Among these materials, zinc oxide (ZnO) has been found to be useful in various other applications [6,7] such as UV resistive coating, piezo-electric devices, varistors, transparent conductive oxide electrode and light emitting devices [7]. ZnO thin film, deposited on silicon substrate with DC reactive magnetron sputtering, has been shown to have an increase in the chemi-resistor sensor response nearly by four orders of magnitude in resistance [8]. ZnO has been shown to exhibit its scope as a practical humidity sensor in the relative humidity range of 6.3–84% along with a response and recovery time of 3 and 12 s, respectively.

On the other hand, ZnO has been widely investigated on various substrates [9,10] including porous templates [11,12] for controlling the particle size and grain boundaries (since these parameters govern and delimit the electrical conduction). ZnO nanoparticles introduced into a mesoporous SiO_2 host enhance the photoluminescence (PL) [13–15]. Zinc oxide nanoparticles/nanowires introduced in the porous anodic alumina host have been shown to enhance the blue emission [16]. Properties of wood-templated zinc oxide, with hierarchical porous structure, have also been reported [17]. In case of nanocrystalline materials, by reducing the grain size, the depletion layer can have similar dimensions as the particle radius, resulting in the adsorption of oxygen in the grains fully depleted of conduction band electrons. Hence, such materials have been proposed for producing highly sensitive gas sensors [18,19].

Motivated by the fact that one of the most important properties affecting the use of any material as a sensor is the actual grain or crystallite size, instead of using a flat template surface, polycrystalline ZnO thin films deposited by RF magnetron sputtering technique, on mesoporous silicon templates were investigated in this work. Porous silicon (PS) is one of the important porous materials since Canham [20] presented the first observation of efficient photoluminescence from PS at room temperature.

Its open structure, tunable pore dimensions, large surface area, convenient surface chemistry, compatibility with the silicon IC technology [21], combined with unique optical and electrical properties, make PS a good candidate for templates [22–25] and an alternative material for gas sensing, operating at relatively low temperatures [26–28]. In this work, ZnO films were deposited on the nanostructured mesoporous silicon layer having a variation of pore sizes in the range of 10–60 nm. The zinc oxide layer has also been deposited on 30 nm thin labyrinth pattern formed on PS surface by electrochemical method. Up to a certain pore dimension of the substrate, zinc oxide crystallite size was found to be dependent on the substrate morphology and the pore dimensions.

Experimental details

PS samples were fabricated by wet electrochemical etching of p^{++}-type Si(0 0 1) wafers with a resistivity of 0.01–0.05 Ω cm. The samples (S1, S2, S3) were prepared with three different concentrations (15:10, 15:70 and 15:85 volumetric ratio, respectively) of hydrofluoric acid (48 wt% HF) and ethanol (98%). The anodization time and current density were kept as 20 s and 10 mA/cm^2 respectively, for all the PS samples. After the fabrication, the samples were rinsed by ethanol and dried in pentane

[29]. In order to study the effect of PS substrate on the physical and transport characteristics of ZnO, thin films were deposited using RF magnetron sputtering. The PS substrate temperature was kept at 300 °C during the deposition of ZnO. Before the deposition of ZnO film, the chamber was evacuated to a pressure of ~9 × 10^{-6} Torr by a turbo molecular pump backed with scroll pump. The films were deposited in argon atmosphere at a base pressure of ~9 × 10^{-3} Torr during the deposition. The RF power was kept to be 150 W with a deposition time of 30 min for each sample. After the ZnO deposition, the combined structures (ZnO–PS) were named as ZS1, ZS2 and ZS3. Deposited films were annealed at 500 °C and further at 700 °C for 1 h in a tubular furnace in argon atmosphere.

The structural properties of the PS and ZnO–PS structures were analyzed using high resolution field emission scanning electron microscope (FESEM: model JSM-7401F). The orientation and crystallinity of the ZnO crystallites were analyzed by XRD spectrometer (Xpert'PRO) equipped with Cu anode X-ray tube (with K_α radiation wavelength of 1.54Å), a flat crystal monochromator and a proportional detector consisting of a cylindrical chamber filled with xenon/methane gas mixture. The angle 2θ ranged from 30° to 65°, with a step of 0.05°. The steady state photoluminescence properties were studied using Varian Fluorescence spectrometer (Cary Eclipse) under the excitation wavelength of 325 nm using a xenon lamp. The surface morphologies of PS substrate and ZnO thin films were analyzed by an atomic force microscopy (AFM) using Vecco Nanoscope IV model. The effect of surface morphology on the transport characteristics was studied with the help of DC resistance measurements. I–V

characteristics were measured between −2 V and 2 V in the lateral configuration shown in the latter part of the manuscript. The metallic contacts were made of silver.

Results and discussion

Top and the cross sectional view of the SEM images of the nanostructured PS films prepared with different electrolyte concentrations with the same current density and anodization time are shown in Fig. 1. In Fig. 1(a, c and e), one can observe the surface of the porous substrates with the average pore sizes of the order of 5, 50 and 20 nm for the sample S1, S2 and S3, respectively.

Table 1
Composition details of PS–ZnO (sample ZS2) structure.

Position of the EDX window	Element	Atomic %
Cross sectional interface of Si–PS (circle point)	Si K-edge O K-edge	72.68 27.32
Cross sectional of ZnO film (rectangle point)	Zn L-edge O K-edge	60.02 39.98

Moreover, the sample S3 shows the labyrinth pattern as show in Fig. 1(e). Their corresponding cross sectional image is given I Fig. 1(b, d and f) showing the thickness of the layers as 447, 147 and 30 nm, respectively. Sample S2 shows the presence of bigge pores than sample S1. The thickness of the porous layer is seen to decrease with the decrease in the concentration of hydrofluoric acid. It is in conformity with the work done by Lehmann [30] where the depth of the pores increases with an increase in HF concentration. It can be further understood by the model proposed by Judge

[31], where the etching rate depends on the relative concentration of HF_2^- and F^-. For the concentrated hydrofluoric acid, the etching is dominated by HF_2^-, as compared to the dilute electrolytes where F prevails. At the same time, the etching rate of HF_2^- is several times more than F^- [32]. Hence, for the same anodization time, dilution of the electrolyte results in the decrease in thickness. On the other hand, several works like Smith and Collins [33], and Ronkel and Schultze [34], explain the formation mechanism through potentiodynamic I–V curves and the maximum peak current is shown to increase with the increase in the HF concentration. This explains the enlargement of the pores (tending towards the electropolishing regime) on diluting the hydrofluoric acid. Further dilution results in the formation of Labyrinth patterns, which have been previously reported on the macroscale by Chazalviel and co-workers [35]. The formation of Labyrinth pattern has been attributed to the formation and dissolution of porous silica at the lower concentration of HF. Oxide formation takes place at the bottom of the nucleation centres (i.e. the pores) and the protons generated by this process diffuse through the porous layer and enable its dissolution. Formation of the pattern is possibly due to the non-uniformity of the dissolution mechanism [35], as the current flows preferentially through the regions where the oxide is thinner, enhancing the rate of the reaction for the porous silica formation.

The effect of annealing of mesoporous silicon substrate has been studied before by several groups [36]. A relative decrease in the pore size and a denser structure as compared to the starting mesoporous layer has been reported, after annealing at high temperatures (between 880 and 1150°C). In the present work, no observable changes were found on annealing similar mesoporous silicon substrates at 700° C. Fig. 2 shows

the top view and the cross sectional scanning electron microscope (SEM) image of the sample ZS2 after annealing at 700 °C. The average thickness of ZnO film, measured by FESEM, is ~125–140 nm with the mean crystallite size close to 40 nm, which is very close to the pore size of S2. This appears to be related to the nucleation of zinc oxide around the pores of PS substrate during the sputtering of ZnO target. This hypothesis will be further confirmed by AFM images and will be discussed in the latter part of the manuscript.

The compositional analysis of the sputtered PS–ZnO-S2 (ZS2) structure was carried out by energy dispersive X-ray (EDX) spectroscopy (shown in the inset of Fig. 2(a)). EDX spectrum of sample ZS2 was taken at two different positions of the cross section indicated by a square and a circle. The details of the atomic ratio of Zn, O, and Si corresponding to the two positions are given in Table 2. The EDX spectrum taken at the interface displays the peaks corresponding to oxygen and silicon, confirming the formation of silicon sub-oxide (SiOx). The presence of oxygen at the PS–silicon interface is due to the formation of native oxide as the samples were stored under normal atmospheric conditions. Apart from that the replacement of the remaining Si–H bonds with Si–O–Si bonds can be expected while annealing the PS–ZnO structure at 700 °C. Similarly, the EDX spectrum of the ZnO film verifies the presence of Zn and the deficiency of oxygen in the film.

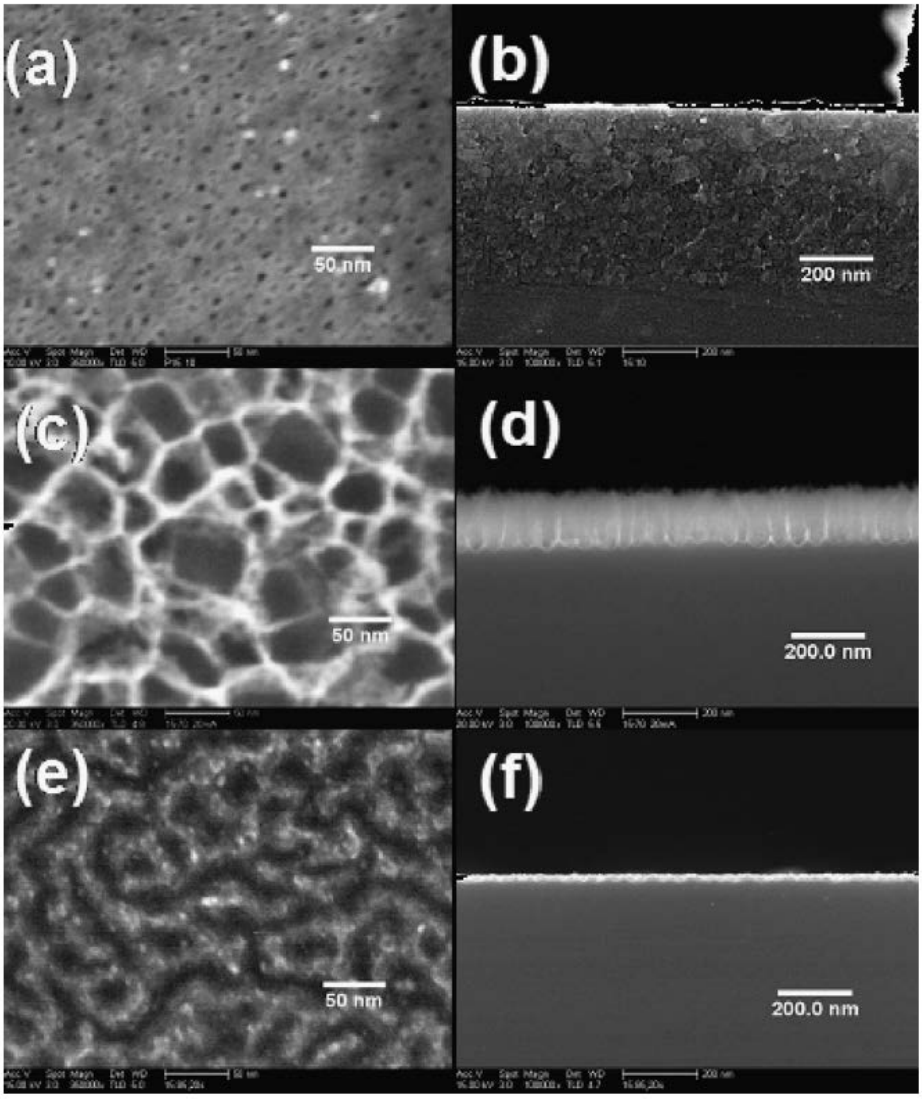

Fig. 1. SEM images of as etched PS: Top view of (a) sample S1 (15_10), (c) sample S2 (15_70) and (e) sample S3 (15_85) and (b), (d) and (f) show their respective cross sectional interface.

Fig. 3 shows the three-dimensional AFM images of (1 μm × 1 μm) of the surface of ZS1, ZS2 and ZS3 samples. It reveals the overall topography of ZnO films deposited over the PS substrate. The spherical features observed on the surface confirm the formation of ZnO nanocrystallites with different features depending on the morphology of the porous substrate. The ZnO film deposited on the low porosity mesoporous silicon (ZS1) substrate is found to have irregular features along with a relatively large value of root-mean-square (rms) roughness ~8 nm.

On enhancing the porosity of the substrate, the nanocrystallites of ZnO are formed with a relatively homogeneous distribution and a decrease in roughness with respect to the nanocrystallites formed on the low porosity substrate is observed. The rms values observed for ZS3 and ZS2 are found to be approximately 5.32 nm and 5.56 nm, respectively. Relatively similar topography of ZS2 and ZS3 concludes that after a certain substrate pore dimensions, the morphology of the sputtered zinc oxide film is independent of the substrate morphology. The observed change in the grain size, distribution and roughness of the ZnO film (ZS2/ZS3 as compared to ZS1), depending on the substrate morphology, can be used as a controlling parameter for changing the structural characteristics of the sputtered zinc oxide layer. Furthermore, the crystalline property as well as the preferred orientation of the film is the main parameter in most of the ZnO devices, which depends on the sputtering parameters and the nature of the substrate [37].

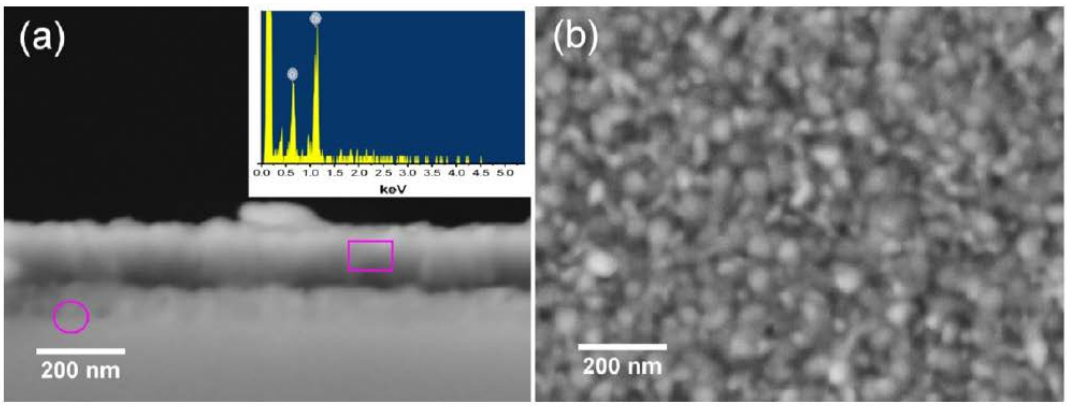

Fig. 2. The SEM images of ZnO/PS film after annealing at 700 °C for 1 h. (a) The cross sectional view showing the thin porous layer over the silicon substrate followed by ZnO layer at the top and (b) top view of the sample. The EDX analysis of sample ZS2 at the position shown by the rectangle (positioned over the ZnO film) is shown as an inset of (a), confirming the presence of oxygen (first peak) and Zn (second peak). Circle at the interface of PS/Si was taken as second position for EDX; corresponding values are given in Table 1.

Fig. 4 shows the typical XRD pattern (corresponding to the sample ZS2) of the ZnO–PS structures annealed at 700 °C. All the samples are shown to exhibit dominant peaks at

2θ = 31.95°, 34.68° and 36.42° corresponding to (1 0 0), (0 0 2) and (1 0 1) planes of ZnO, respectively. The XRD pattern of ZnO reveals a hexagonal Wurtzite structure and polycrystalline nature (JCDPS card number: 36-1451). The films are oriented perpendicular to the substrate surface in c-axis and with respect to the ZnO powder demonstrate a small peak shift (0.13) towards the higher diffraction angle which is mainly associated with the induced strain in the films [38]. The c-axis orientation can be understood due to the fact that c-plane of the zinc oxide crystallites corresponds to the densest packed plane.

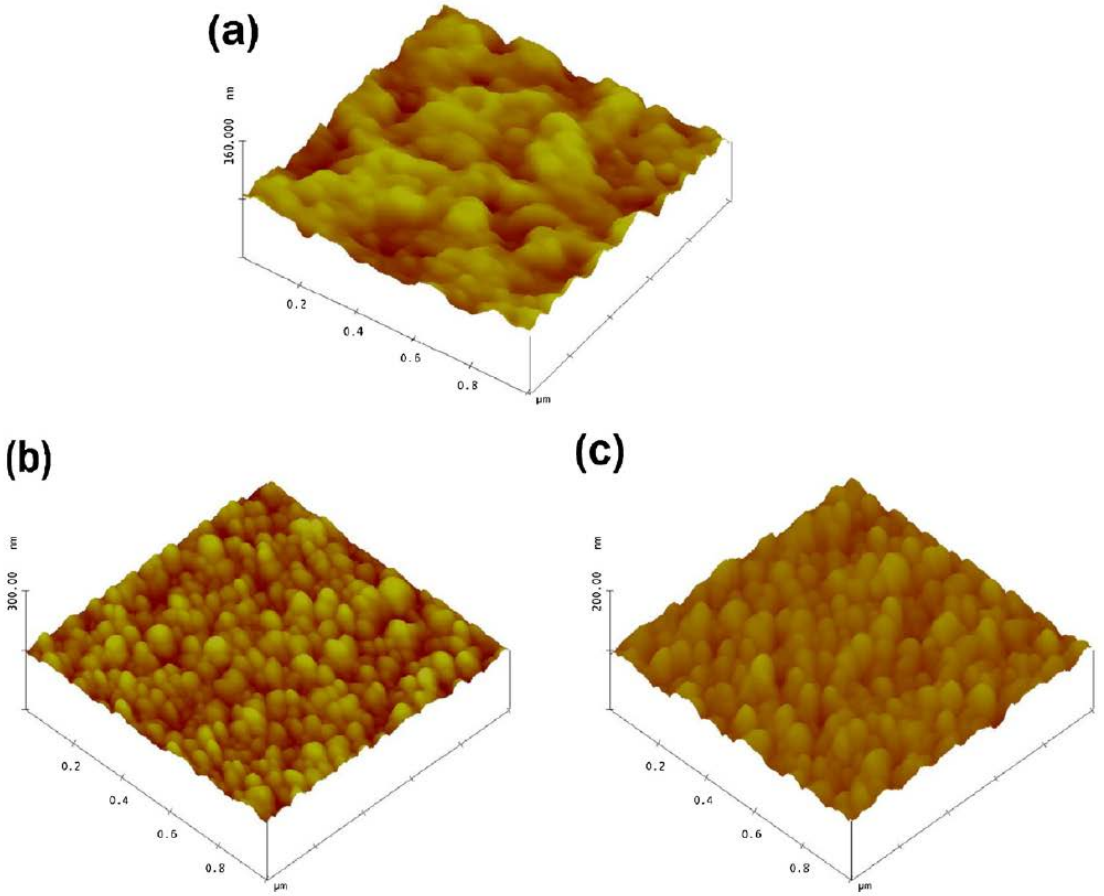

Fig. 3. Atomic force microscopy images of the surface of the ZnO layer deposited on different mesoporous substrates S1, S2 and S3 (shown in Fig. 1) (a) ZS1, (b) ZS2 (c) ZS3.

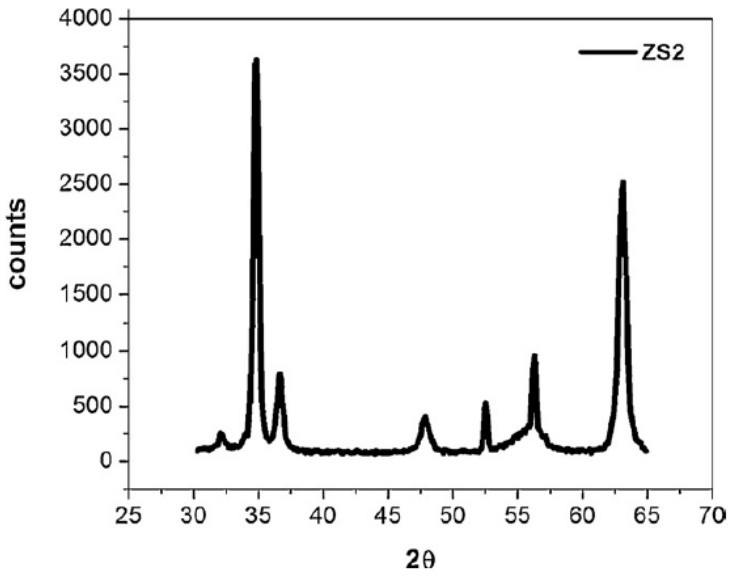

Fig. 4. Typical XRD spectra of annealed (at 700 °C) ZnO–PS structure (ZS2).

The average size of the crystallites for ZS2 is calculated using the Scherrer's formula and is found to be 20.47 nm. The lattice constants, a = b = 3.233 Å and c = 5.185 Å are calculated (ZS2) from the observed XRD pattern and the details are summarized in Table 2. The peak at 2θ = ~56° corresponds to PS which is present in all the samples.

PL spectra of the ZnO–PS structures are shown in Fig. 5. For understanding the mechanism involved in the emission processes, it can be de-convoluted into various PL emission bands. PL emission in the UV region around 390 nm (390, 386 and 401 nm for the ZS1, ZS2 and ZS3, respectively) could be attributed to the near band edge excitonic recombinations [39] from ZnO film. The shift in the peak position could be attributed to the stresses present in ZnO crystallites. The sample ZS1 shows the maximum PL intensity around 390 nm along with the emission from 695 to 800 nm, as compared to the samples ZS2 and ZS3. The ratio of UV to visible emission has been considered as a key criterion to evaluate the crystalline quality of ZnO. On comparison, ZS1 exhibits

very strong UV emission along with some visible emission (UV–vis ratio = 8.37), as compared to almost similar values for ZS2 and ZS3 as 5.05 and 5.08 respectively [40]. Consequently, a strong UV emission and weak green emission from ZnO could be attributed to good crystalline quality of ZnO film. Green emission has been reported as the most common and most controversial band in zinc oxide [41]. Many different hypotheses have been proposed to explain the green emission but there is still no consensus [42]. During the past years, the green PL emission from 500 to 530 nm is considered to be due to the deep level defects [43]. Some groups have proposed Zn vacancies [44], and oxygen antisite [45] as the possible source of green emission. The most commonly cited hypothesis for the origin of green emission remains singly ionized oxygen vacancy [46]. In our work, these defects are considered to be arising from the oxygen vacancies in the ZnO lattice [46] as they could be corroborated with the EDX analysis showing the deficiency of oxygen in the ZnO layer (see inset of Fig. 2(a) and Table 1). Recently its mechanism has been explained by Dijiken et al. [47], through the transition of a photogenerated electron from a shallow level, close to the conduction band edge, to a deeply trapped hole (a $V_{\bar{0}}^{**}$ centre) resulting in the visible emission. The surface trapped hole can tunnel into the particle, resulting in the creation of a $V_{\bar{0}}^{**}$ centre (recombination centre for visible emission), due to its recombination with an electron in an oxygen vacancy ($V_{\bar{0}}^{*}$).

On the other hand, PL in the higher wavelength region from 695 to 800 nm range is due to PS substrate used as the template. ZS1 shows a relatively higher emission due to the fact that the porous layer thickness in sample S1 is an order of magnitude more than the other two porous layers, S2 and S3 (as shown in Fig. 1).

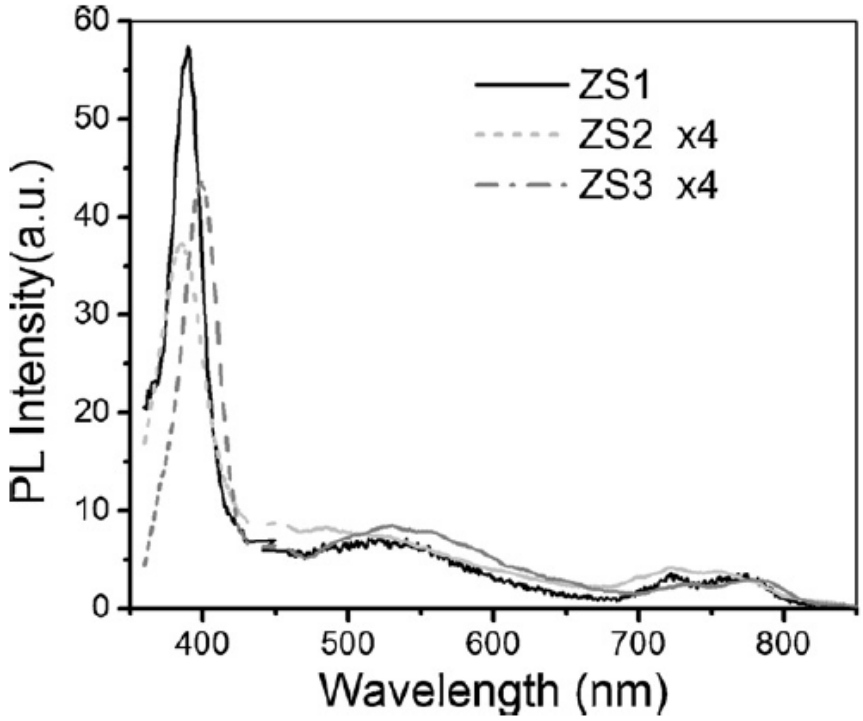

Fig. 5. PL spectra of annealed ZnO–PS structures ZS1, ZS2, and ZS3.

Along with the physical and optical characteristics, electrical properties have been studied to investigate and confirm the influence of surface morphology on the tunability of the sensing performance. Resistance is a measurable parameter and normally sufficient for comparing the sensing performance [1,48]. Fig. 6 shows the dependence/tunability of I–V characteristics, performed in lateral configuration (inset of Fig. 6) at room temperature, of thin zinc oxide layer on the morphology of the film. The I–V characteristics were measured at the sweep rate of 150 mV/s. Fig. 6 demonstrates the non-ohmic electrical response, which is normally attributed to the formation of Schottky barriers at the Ag–ZnO interfaces, due to the higher work function of silver (4.73 eV) than ZnO (4.5 eV). It was seen that the samples ZS2 and ZS3 show higher forward/reverse current than the sample ZS1 due to the fact that an enhanced surface

area of ZS2/ZS3 (Ref. to Fig. 3) causes more contact between the metal and the zinc oxide nanocrystallites and hence more rectifying behavior is observed.

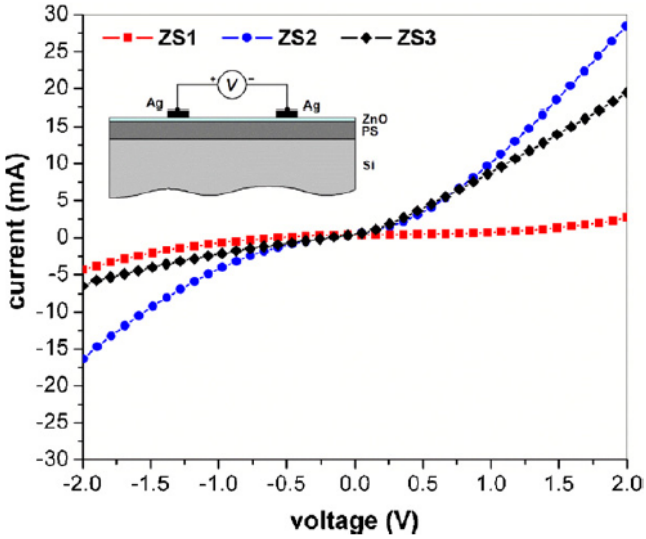

Fig. 6. Current–voltage (I–V) curves of ZnO–PS structures (ZS1, ZS2 and ZS3) measured at room temperature, from 0 to −2 V, 0 to 2 V with a sweep rate of 150 mV/s. Upper inset shows the schematic of the configuration used for I–V characteristics and DC resistance measurements.

In order to quantify the deviation from the Schottky behavior, the rectifying factor (IF/IR) was calculated at 1 V and was found to be 0.87, 2.32 and 3.87 for ZS1, ZS2 and ZS3, respectively.

Conclusions

Our experimental results indicate that the spacial distribution of zinc oxide nanocrystallites in RF sputtered zinc oxide layer can be controlled by tuning the porosity and the pore size distribution of the porous silicon substrate. Monodisperse distribution of zinc oxide crystallites can be achieved by depositing it over the PS substrate with regular pore size distribution. We have also demonstrated the use of zinc oxide film, over the porous silicon nanostructures, in altering the transport properties. The

discovery of the tunable electrical response and the controlled spacial distribution of the zinc oxide nanocrystallites, through mesoporous substrates, opens a versatile route to enhance the sensing response of different semiconducting oxides which consequently has many important technological implications.

Acknowledgements

Authors are thankful to DST, Govt. of India and CONACyT, Mexico for providing the bilateral exchange project (DST/INT/MEX/RPO- 09/2008 and Mexico-India J000.0374). One of the authors (VA) also acknowledges the partial support given by CONCyT project number 128593 while the author (YK) acknowledges the CONACyT support (179496) for doctoral scholarship. We acknowledge the technical support provided by CIMAV (Wilber Antunez Flores, Enrique Torres) for extending the use of SEM/XRD facility from the National Nanotechnology Laboratory (NanoTech) and Daniel Bahena for AFM images. We acknowledge the useful discussions made with Dr. U.Pal from Instituto de Fisica, BUAP, Mexico).

References

[1] P.T. Mosely, B.C. Tofield, Solid State Gas Sensor, Adam Hilger, Bristol/ Philadelphia, 1987; U. Bazill, Diebold, Prog. Surf. Sci. 79 (2005) 47.

[2] S.K. Hazra, S. Basu, Sens. Actuators B 115 (2006) 403.

[3] G. Sberveglieri, Sens. Actuators B 23 (1995) 103;

A. Erol, S. Okur, B. Comba, O. Mermer, M.C. Arikan, Sens. Actuators B 145 (2010) 174.

[4] N. Barsan, U. Weimar, J. Electroceram. 7 (2001) 143.

[5] M.J. Vellekoop, C.C.O. Visser, P.M. Sarro, A. Venema, Sens. Actuators A: Phys. 23 (1990) 1027.

[6] R.P. Ried, E. Kim, D.M. Hong, R.S. Muller, J. Microelectromech. Syst. 2 (1993) 111; Y. Ito, K. Kuchida, K. Sugawara, H. Takeuchi, IEEE Trans. Ultrason. Ferroelectr. Frequency Control 42 (1995) 316.

[7] A.B. Djurisic, A.M.C. Ng, X.Y. Chen, Prog. Quantum Electron. 34 (2010) 191; G. Hu, S.Q. Li, H. Gong, Y. Zhao, et al., J. Phys. Chem. C 113 (2009) 751.

[8] P.K. Kannan, R. Saraswathi, J. Bosco, B. Rayappan, Sens. Actuators A: Phys. 164 (2010) 8.

[9] H.J. Ko, Y.F. Chen, Z. Zhu, T. Yao, I. Kobayashi, H. Uchiki, Appl. Phys. Lett. 76 (2000) 1905.

[10] A. Ohtomo, K. Tamura, K. Saikusa, T. Takahashi, T. Makino, Y. Segawa, H. Koinuma, M. Kawasaki, Appl. Phys. Lett. 75 (1999) 2635.

[11] W.H. Zhang, J.L. Shi, L.Z. Wang, D.S. Yan, Chem. Mater. 12 (2000) 1408.

[12] Y. Li, G.W. Meng, L.D. Zhang, F. Phillipp, Appl. Phys. Lett. 76 (2000) 2011.

[13] C.M. Mo, Y.H. Li, Y.S. Liu, Y. Zhang, L.D. Zhang, J. Appl. Phys. 83 (1998) 4389.

[14] R.G. Singh, Fouran Singh, V. Agarwal, R.M. Mehra, J. Phys. D: Appl. Phys. 40 (2007) 3090.

[15] R.G. Singh, Fouran Singh, D. Kanjilal, V. Agarwal, R.M. Mehra, J. Phys. D: Appl. Phys. 42 (2009) 062002.

[16] T. Gao, G. Meng, Y. Tian, S. Sun, X. Lui, L. Zhang, J. Phys.: Condens. Matter 14 (2002) 12651.

[17] L. Zhaoting, F. Tongxiang, J. Ding, D. Zhang, Q. Guo, H. Ogawa, Ceram. Int. 34 (2008) 69.

[18] G. Sberveglieri, Sens. Actuators B 23 (1995) 103;
V. Guidi, et al., Sens. Actuators B 57 (1999) 197;
J. Kanungo, H. Saha, S. Basu, Sens. Actuators B: Chem. 147 (2010) 128.

[19] Y. Shimizu, M. Egashira, MRS Bull. 6 (1999) 18.

[20] L.T. Canham, Appl. Phys. Lett. 57 (1990) 1046.

[21] G. Barillaro, A. Nannini, F. Pieri, Sens. Acuators B 93 (2003) 263.

[22] D.S. Xu, G.L. Guo, L.L. Gui, Y.Q. Tang, Z.J. Shi, Z.X. Jin, Z.N. Gu, W.M. Liu, X.L. Li, G.H. Zhang, Appl. Phys. Lett. 75 (1999) 481.

[23] V. Chin, B.E. Collins, M.J. Sailor, S. Bhatia, Nanostruct. Adv. Mater. 13 (2001) 1877.

[24] V. Agarwal, M.E. Mora-Ramos, B. Alvarado Tenorio, Photonics Nanostruct.: Fundam. Appl. 6 (2009) 63;
J. Escorcia-Garcia, O. Sarracino Martínez, J.M. Gracia-Jiménez, V. Agarwal, J.

Phys. D: Appl. Phys. 42 (2009) 145101.

[25] J.O. Estevez, J. Arriaga, A.M. Blas, V. Agarwal, Appl. Phys. Lett. 94 (2009) 61914;

J.O. Estevez, J. Arriaga, A.M. Blas, V. Agarwal, Appl. Phys. Lett. 93 (2008) 191915.

[26] S.E. Lewis, J.R. DeBoer, J.L. Gole, P.J. Hesketh, Sens. Actuators B: Chem. 110 (2005) 54.

[27] J. Mizsei, Thin Solid Films 515 (2007) 8310.

[28] S. Khoshnevis, R.S. Dariani, M.E. Azim-Araghi, Z.B. Bayindir, K. Robbie, Thin Solid Films 515 (2006) 2650.

[29] O. Belmont, D. Bellet, Y. Brechet, J. Appl. Phys. 79 (1996) 7586;

L.T. Canham (Ed.), Properties of Porous Silicon, INSPEC, The Institution of Electrical Engineers, London, United Kingdom, 1997, pp. 38–43.

[30] V. Lehmann, J. Electrochem. Soc. 140 (1993) 2836.

[31] J.S. Judge, J. Electrochem. Soc. 118 (1971) 1772.

[32] M. Matsumura, H. Fukidome, J. Electrochem. Soc. 143 (1996) 2683;

S. Cattarin, I. Frateur, M. Musiani, B. Tribollet, J. Electrochem. Soc. 147 (2000) 3277; L. Pavesi, V. Mulloni, J. Lumin. 80 (1999) 43.

[33] R.L. Smith, S.D. Collins, J. Appl. Phys. 71 (1992) R1.

[34] F. Ronkel, J.W. Schultze, J. Porous Mater. 7 (2000) 11.

[35] M.A. Amin, S. Frey, F. Ozanam, J.-N. Chazalviel, Electrochim. Acta 53 (2008) 4485.

[36] N. Ott, M. Nerding, G. Müller, R. Brendel, H.P. Strunk, Phys. Stat. Solidi (A) 197 (2003) 93;

M. Hajji, M. Khardani, N. Khedher, H. Rahmouni, B. Bessaı¨s, H. Ezzaouiaa, H. Bouchriha, Thin Solid Films 511 (2006) 235.

[37] Y. Lee, Y. Kim, H. Kim, J. Mater. Res. 13 (1998) 1260.

[38] B.D. Cullity, Elements of X-ray Diffraction, 2nd ed., Addison-Wesley Publishing Company Inc., US, 1978.

[39] X.L. Wu, G.G. Siu, C.L. Fu, H.C. Ong, Appl. Phys. Lett. 78 (2001) 2285.

[40] M. Wang, L. Zhang, Mater. Lett. 63 (2009) 301.

[41] A.B. Djurisic, Y.H.L. euang, Small 2 (8–9) (2006) 944.

[42] A.B. Djurisic, A.M.C. Ng, X.Y. Chen, Prog. Quantum Electron. 34 (2010) 191.

[43] B.X Lin, Z.X. Fu, Y.B. Jia, Appl. Phys. Lett. 79 (2001) 943.

[44] Q.X. Zhao, P. Klason, M. Willander, H.M. Zhong, W. Lu, J.H. Yang, Appl. Phys. Lett. 85 (2004) 1601.

[45] B. Lin, Z. FU, Y. Jia, Appl. Phys. Lett. 79 (2001) 943.

[46] K. Vanheusden, C.H. Seager, W.L. Warren, D.R. Tallant, J.A. Voigt, Appl. Phys.

Lett. 68 (1996) 403.

[47] A.V. Dijiken, E.A. Meulenkamp, D. Vanmaekelbergh, A. Meijerink, J. Phys. Chem. B 104 (2000) 1715.

[48] M.J. Madou, S.R. Morrison, Chemical Sensing with Solid State Devices, Academic Press, Inc., London, 1989